CRS4

Center for Research, Development
and Advanced Studies in Sardinia

Uta - (CA)

ENEA-MURST Programme

Objective 4

Development and Implementation of Turbulence Models in the Combustion Code Ares

by:

M. Mulas, E. Stalio and M. Talice

Computational Fluid Dynamics Area

Abstract

This report describes the R&D activities carried out under the ENEA-MURST programme, objective 4. Three more turbulence models (the *RNG* $\kappa - \epsilon$, the one-equation Spalart & Allmaras and the Wilcox $\kappa - \omega$) have been implemented into the **Ares** combustion code. They represent state-of-the-art models that have demonstrated over the past decade their superior accuracy, robustness as well as ease of implementation with respect to the class of $\kappa - \epsilon$ models. The first chapter describes the models formulations. In chapter 2 the three models have been validated against three well known test cases.

Particular attention has been dedicated to coupling the one-equation turbulence model by Spalart & Allmaras to the TFC premixed combustion model, for two computed turbulence scales are needed to evaluate the turbulent flame velocity and one-equation models provide one turbulent scale only.

For validating the correct models implementations, two simple cold test cases have been chosen, namely the turbulent boundary layer over a flat plate, and a well documented turbulent flow over a backward facing step. Finally the Moreau combustor test case have been used for the validation of the models for premixed combustion flow.

The state-of-the-art turbulence models implemented should allow the combustion code **Ares** to increase its ability to correctly compute complex turbulent premixed reactive flows in real combustors, which is the objective of the next project tasks.

Contents

1 Implementation of turbulence models **2**

1.1 The RNG $\kappa - \epsilon$ model . . . 2

1.1.1 Introduction . . . 2

1.1.2 Model formulation . . . 2

1.2 The one-equation Spalart & Allmaras model . . . 4

1.2.1 Introduction . . . 4

1.2.2 Model formulation . . . 4

1.2.3 Coupling the S&A model to the TFC combustion model . . 6

1.3 The Wilkox' $\kappa - \omega$ model in *log* formulation . . . 8

1.3.1 Introduction . . . 8

1.3.2 Model formulation . . . 9

2 Validation **12**

2.1 Turbulent flow over a flate plate . . . 12

2.1.1 Description . . . 12

2.1.2 Test case set-up . . . 12

2.1.3 Results . . . 12

2.2 Backward Facing Step . . . 15

2.2.1 Description . . . 15

2.2.2 Test case set-up . . . 15

2.2.3 Results . . . 16

2.3 Moreau Combustor . . . 27

2.3.1 Description . . . 27

2.3.2 Test case set-up . . . 28

2.3.3 Results . . . 28

References **34**

1 Implementation of turbulence models

In the present chapter the implementation of the three new turbulence models into **Ares** combustion code will be described. All models have diffusion and source terms discretized with second order accurate schemes, and convective fluxes with first order upwind schemes.

1.1 The RNG $\kappa - \epsilon$ model

1.1.1 Introduction

In the classical two equations $\kappa - \epsilon$ model, the turbulence length scale and the time scale are built up starting from the turbulent kinetic energy κ and the turbulent dissipation rate ϵ, which are obtained by solving the two corresponding transport equations. Then the Reynolds stress tensor is represented by an eddy viscosity model constructed from length and time scales based on κ and ϵ, namely $\mu_t = C_\mu \kappa^2/\epsilon$. The major criticism against this model is that it is not derived from the Navier-Stokes equation in a systematic fashion. In particular the equation for ϵ has little phisycal ground. Yakhot and Orszag [1] derived a version of the $\kappa - \epsilon$ model by using Renormalization Group (RNG) methods. By following this approach, an expansion is made about an equilibrium state with known Gaussian statistics by making use of the correspondence principle, wherein the effects of mean strains are represented by a random force. Bands of high wave numbers (namely, the small scales) are systematically removed and space is re-scaled. It has to be noted as the removal of only the smallest scales gives rise to subgrid scales models typical of large eddy simulations whereas the removal of successively larger scales leads to Reynolds stress models. At high Reynolds number the RNG model by Yakhot and Orzag is of the same general form of the standard $\kappa - \epsilon$ model; however constants are calculated explicitly and an extra term appears in the ϵ equation.

1.1.2 Model formulation

The model's equations write as:

$$\frac{\partial \rho \kappa}{\partial t} + \frac{\partial \rho \kappa u_j}{\partial x_j} = \frac{\partial}{\partial x_j}\left[\left(\mu + \frac{\mu_t}{\sigma_\kappa}\right)\frac{\partial \kappa}{\partial x_j}\right] + \rho P - \rho \epsilon \tag{1}$$

$$\frac{\partial \rho \epsilon}{\partial t} + \frac{\partial \rho \epsilon u_j}{\partial x_j} = \frac{\partial}{\partial x_j}\left[\left(\mu + \frac{\mu_t}{\sigma_\epsilon}\right)\frac{\partial \epsilon}{\partial x_j}\right] + \frac{\epsilon}{\kappa}\left(C_1 \rho P - C_2 \rho \epsilon\right) - R \tag{2}$$

$$\mu_t = C_\mu \rho \frac{\kappa^2}{\epsilon}$$

$$P = \frac{\kappa^2}{\epsilon} A - \kappa B$$

$$A = C_\mu \left[\frac{\partial u_i}{\partial x_j}\left(\frac{\partial u_i}{\partial x_j} + \frac{\partial u_i}{\partial x_j}\right) - \frac{2}{3}\left(\frac{\partial u_i}{\partial x_i}\right)^2\right] \geq 0$$

$$B = \frac{2}{3}\frac{\partial u_i}{\partial x_i}$$

The additional term **R** which appears in the RNG ϵ equation writes:

$$R = \frac{C_\mu \rho \eta^3 \left(1 - \frac{\eta}{\eta_0}\right)}{1 + \beta \eta^3}\frac{\epsilon^2}{\kappa}$$

where it is:

$$\eta = \sqrt{\frac{P}{\mu_t}}\frac{\kappa}{\epsilon}$$

Unlikely the standard $\kappa - \epsilon$ model, RNG model is valid for low Reynolds flow regime also and ϵ equation can be integrated down to solid walls. RNG theory provides a differential equation for turbulent viscosity, which can be written as:

$$d\left(\frac{\rho^2 \kappa}{\sqrt{\epsilon \mu}}\right) = 1.72 \frac{\hat{\nu}}{\sqrt{\hat{\nu}^3 - 1 + C_\nu}} d\hat{\nu}$$

$$\hat{\nu} = \frac{\mu_t}{\mu}$$

$$C_\nu \approx 100$$

RNG theory provides also a formula to compute the inverse of the turbulent Prandtl numbers σ_κ and σ_ϵ:

$$\left|\frac{\sigma_{\kappa,\epsilon} - 1.3929}{\sigma_0 - 1.3929}\right|^{0.6321}\left|\frac{\sigma_{\kappa,\epsilon} - 2.3929}{\sigma_0 - 2.3929}\right|^{0.3679} = \frac{\mu}{\mu_t} \tag{3}$$

In the high-Reynolds number limit (namely, the usual condition in industrial combustion processes), turbulent viscosity reduces to the formulation used in the standard model, thus:

$$\mu_t = C_\mu \rho \frac{\kappa^2}{\epsilon}$$

and the inverse of Prandtl numbers are the asymptotic solution of formula 3:

$$\sigma_\kappa = \sigma_\epsilon = 1.393$$

1.2 The one-equation Spalart & Allmaras model

1.2.1 Introduction

In the last few years, the Spalart & Allmaras one-equation turbulence model, presented in 1992 [2], has become very popular in the CFD community. The model presents several advantages with respect to both algebraic and two-equation models: firstly, it is "local" and therefore well suited to block-structured as well as unstructured Navier-Stokes codes; and secondly it is easy to use, demanding trivial boundary conditions and showing no stiffness, typical of the class of two-equation $\kappa-\epsilon$ models expecially when equipped with low Reynolds number formulations for the near wall region. The model solves for a modified turbulent viscosity ν and it is constructed as three nested models: for free shear flows, for near wall region and high Reynolds number (the *log* region of the boundary layer), and for near wall region and finite Reynolds number (which allow integration till the laminar viscous sub-layer). Depending on the mesh resolution near solid boundaries, the various nested models may become passive, so no strict requirement exists on y^+. Several comparative studies has demonsatrated the model's robustness and accuracy [3], [4], [5].

When coupling the S&A model with the TFC premixed combustion model, some care has been put in deriving a turbulent time scale not directly obtained integrating a second turbulent variable as in the cases of two-equation models.

1.2.2 Model formulation

The S&A model solves for a modified turbulent eddy viscosity ν and the model equation reads as:

$$\frac{D\nu}{Dt} = c_{b1} S \nu + \frac{1}{\sigma}\left[\frac{\partial}{\partial x_j}\left((\nu+\nu)\frac{\partial \nu}{\partial x_j}\right) + c_{b2}\frac{\partial \nu}{\partial x_k}\frac{\partial \nu}{\partial x_k}\right] - c_{w1} f_w \left[\frac{\nu}{d}\right]^2 \tag{4}$$

where the three terms on the right hand side represent the source, the diffusion and the destruction term. It has to be noticed that the diffusion presents an extra, non conservative term. For an easier implementation into the Finite-Volume code, the model equation has been reformulated as follows (multiplying by the density ρ):

$$\begin{aligned}\frac{\partial \rho\nu}{\partial t} + \frac{\partial \rho\nu u_j}{\partial x_j} = \quad & c_{b1} S \rho\nu \; - \; c_{w1} f_w \rho \left[\frac{\nu}{d}\right]^2 \; + \; \frac{1+c_{b2}}{\sigma}\frac{\partial}{\partial x_j}\left(\rho\nu\frac{\partial \nu}{\partial x_j}\right) \\ & + \frac{1}{\sigma}\frac{\partial}{\partial x_j}\left(\mu\frac{\partial \nu}{\partial x_j}\right) \; - \; \frac{c_{b2}}{\sigma}\rho\nu\frac{\partial}{\partial x_j}\left(\frac{\partial \nu}{\partial x_j}\right)\end{aligned} \tag{5}$$

The turbulent viscosity is then given by $\nu_t = \nu f_{v1}$, with:

$$f_{v1} = \frac{\chi^3}{\chi^3 + c_{v1}^3} \tag{6}$$

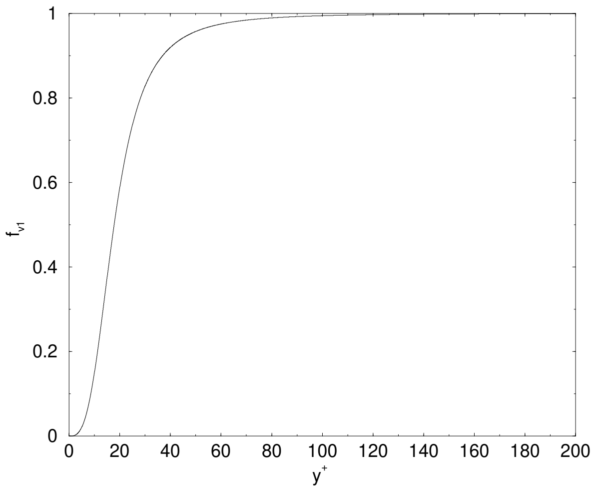

Figure 1: Function fv1 vs y^+

The form of the function f_{v1} versus y^+ is depicted in figure 1. The figure 1 shows that in the region of high y^+ ($y^+ > 60$) the function f_{v1} is approximatelly equal to one, whereas f_{v1} goes to zero for the lowest values of y^+, resulting in a smooth linear behaviour of ν at solid walls. Constants and other quantities which appear in the model equation 5 are listed below.

$$\nu_t = \nu f_{v1}; \qquad f_{v1} = \frac{\chi^3}{\chi^3 + c_{v1}^3}; \qquad \chi \equiv \frac{\nu}{\nu}$$

$$S \equiv S + \frac{\nu}{k^2 d^2} f_{v2}; \qquad f_{v2} = 1 - \frac{\chi}{1 + \chi f_{v1}} \qquad c_{w1} = \frac{c_{b1}}{k^2} + \frac{1 + c_{b2}}{\sigma}$$

where ν is the molecular viscosity, S is the magnitude of the vorticity, and d is the distance to the closest wall.

$$f_w = g \left[\frac{1 + c_{w3}^6}{g^6 + c_{w3}^6} \right]^{1/6} \qquad g \equiv r + c_{w2} \left(r^6 - r \right); \qquad r \equiv \frac{\nu}{S k^2 d^2}$$

$$\sigma = 2/3 \qquad c_{b1} = 0.1355 \qquad c_{b2} = 0.622 \qquad c_{v1} = 7.1 \qquad k = 0.41$$

For large r, f_w reaches a constant, so large value of r can be truncated to 10 or so.

1.2.3 Coupling the S&A model to the TFC combustion model

The turbulent flame velocity in the TFC premixed combustion model is expressed as ([6] and [7]):

$$U_t = A\,G\,u'^{\frac{3}{4}} U_l^{\frac{1}{2}} \chi_t^{-\frac{1}{4}} l_t^{\frac{1}{4}} a \tag{7}$$

where l_t is the integral length scale, χ_t is the thermal diffusivity, U_l is the laminar flame velocity.

The local intensity of velocity fluctuations u' and the integral length scale l_t can be expressed in terms of turbulent kinetic energy and its dissipation rate:

$$u' = \sqrt{\frac{2}{3}k} \qquad\qquad l_t = c_d \frac{\kappa^{\frac{3}{2}}}{\epsilon} \tag{8}$$

which are available when using any two-equation turbulence model. The model constant A is set equal to 0.51, $c_d = 0.2$ and χ_t and U_l are test case dependent and determined in the preprocessing phase. The stretching factor G is calculated from the expression:

$$G = \frac{1}{2}\,\mathrm{erfc}\Big(-\frac{1}{\sqrt{2\sigma}}\Big[\ln\Big(\frac{\epsilon_{cr}}{\tilde{\epsilon}}\Big) + \frac{\sigma}{2}\Big]\Big) \tag{9}$$

where erfc denotes the *complementary error function*, $\sigma = \mu \ln(l_t/\eta)$ the *logarithm* of the standard deviation of the instantaneous value of ϵ about his average value $\tilde{\epsilon}$.

When using the Spalart & Allmaras turbulence model, only a single transport equation for one turbulence quantity is solved, a second relation must then be available in order to compute the turbulent flame speed in terms of two independent kinematic scales such as u' and l_t.

Turbulent flame speed (7), by dropping the stretching factor G, can be expressed in terms of the turbulent quantities κ and ϵ:

$$U_t = \; c_1\, c_2 \;\; \kappa^{\frac{3}{4}} \; \epsilon^{-\frac{1}{4}} \tag{10}$$

where c_1 is a dimensionless constant ($c_1 \simeq 0.293$), c_2 is a macroscopic case-dependent constant ($c_2 \sim \tau_{ch}^{-\frac{1}{4}}$) and their analytical expression is:

$$c_1 = (2/3)^{\frac{3}{8}}\, c_d^{\frac{1}{4}}\, A \qquad\qquad c_2 = U_l^{\frac{1}{2}}\, \chi_t^{-\frac{1}{4}} \tag{11}$$

In order to find an expression for U_t in the Spalart & Allmaras case, an eligible turbulent quantity to be coupled with ν_t is the inverse of the vorticity magnitude; from the implementation point of view the use of this quantity is particularly appealing since it has already been used to evaluate the production term of equation 5 and can be regarded as a turbulent time scale:

$$\tau_t \sim \frac{1}{|\Omega|} \tag{12}$$

U_t can then be expressed as:

$$U_t = \; c_1 \, c_2 \, c_3 \; \nu_t^{\frac{1}{2}} \; |\Omega|^{\frac{1}{4}} \tag{13}$$

the dimensionless constant c_3 is $\mathcal{O}(c_3) = 1$ and has to be determined through comparison with the $\kappa - \epsilon$ results: the equation 14 should hold all over the computational domain with the chosen value of c_3.

$$c_3 \simeq \frac{\kappa^{\frac{3}{4}} \; \epsilon^{-\frac{1}{4}}}{\nu_t^{\frac{1}{2}} \; |\Omega|^{\frac{1}{4}}} \tag{14}$$

After a value for c_3 is determined, κ, ϵ and the related turbulent quantities can be obtained by adding the expression for the eddy viscosity in the $\kappa - \epsilon$ model (15) to the equation 14:

$$\nu_t = c_\mu \, \frac{\kappa^2}{\epsilon} \tag{15}$$

where $c_\mu = 0.09$. Thus turbulent quantities κ and ϵ are given by:

$$\epsilon = \; c_3^8 \; c_\mu^3 \; \nu_t \; |\Omega|^2 \qquad\qquad \kappa = \sqrt{\frac{\nu_t \, \epsilon}{c_\mu}} \tag{16}$$

Once the ϵ field is known, the stretching factor can be determined straightforward by equation 9.

The relation between the turbulent time scale in a Spalart & Allmaras calculation $\tau_t \sim |\Omega|^{-1}$ and in a $\kappa - \epsilon$ one ($\tau_t \sim \kappa/\epsilon$) is:

$$\frac{1}{|\Omega|} = \; c_3^4 \; c_\mu^2 \; \frac{\kappa}{\epsilon} \tag{17}$$

equation 17 proceeds from equations 14 and 15.

1.3 The Wilkox' $\kappa - \omega$ model in *log* formulation

1.3.1 Introduction

The $k-\omega$ model by Wilcox [8], unlike any other two-equation model, does not involve damping functions and allows simple Dirichlet boundary conditions to be specified. Because of its simplicity, the $k-\omega$ model is superior to other models, especially with regard to numerical stability. It is accurate in predicting the mean flow profiles and the wall skin friction, even though it does not predict (as many other models) the correct asymptotic behaviour close to the wall. Furthermore, the behaviour of the $k-\omega$ model in the logarithmic region is superior to that of $\kappa-\epsilon$ model in equilibrium adverse pressure gradient flows and in compressible flows. One point of criticism is that the $k-\omega$ model has a very strong sensitivity to the arbitrary free stream values specified for ω outside the boundary layer. However, in combustion test cases inflow boundaries are often sufficiently confined, as opposed to external aerodynamics test cases, so that this deficiency does not exhibit.

The complete $k-\omega$ Wilcox model can be formulated as

$$\frac{\partial \rho k}{\partial t} + \frac{\partial \rho k u_j}{\partial x_j} = \frac{\partial}{\partial x_j}\left[(\mu + \sigma_k \mu_t)\frac{\partial k}{\partial x_j}\right] + S_k \tag{18}$$

$$\frac{\partial \rho \omega}{\partial t} + \frac{\partial \rho \omega u_j}{\partial x_j} = \frac{\partial}{\partial x_j}\left[(\mu + \sigma_\omega \mu_t)\frac{\partial \omega}{\partial x_j}\right] + S_\omega \tag{19}$$

where,

$$S_k = \mu_t (PROD_k - \beta^* DESTR_k) \tag{20}$$

$$S_\omega = \rho(\gamma PROD_\omega - \beta DESTR_\omega) \tag{21}$$

$$PROD_k = PROD_\omega = \frac{\tau_{ij}^R}{\mu_t}\frac{\partial u_i}{\partial x_j} - \frac{2}{3}\omega\frac{\partial u_i}{\partial x_i}\delta_{ij} \tag{22}$$

$$DESTR_k = DESTR_\omega = \omega^2 \tag{23}$$

$$\mu_t = \frac{\rho k}{\omega} \tag{24}$$

In the Wilcox model $\sigma_k = 0.5$, $\sigma_\omega = 0.5$, $\beta = 3/40 = 0.075$, $\gamma = 5/9 \approx 0.55$, $\beta^* = 9/100$.

1.3.2 Model formulation

One of the main problems encountered when using the $k-\omega$ model (as any other two-equation model) is the stiffness ot the whole system due to the ω equation. Generally, good initial conditions are needed in order to obtain a converged solution. Moreover, sometimes during the transient, unphysical negative values of k or ω are obtained in some points; this gives rise to a negative turbulent viscosity and can trigger dangerous numerical instabilities. A non-standard implementation of the model, whereby the logarithm of ω rather than ω itself is used as unknown, has been found very useful to enhance the stabilty. This formulation was successfully implemented in the CRS4 compressible code **Karalis** [9], and showed increased accuracy as well as robustness.

Starting from eqs. 18 to 24, with the positions:

$$\breve{\omega} = ln(\omega) \Rightarrow \omega = e^{\breve{\omega}}$$

the $log(\omega)$ formulation can be formally derived.

For a generic variable a, the following identities hold:

$$\frac{\partial a\omega}{\partial x} = \frac{\partial a e^{\breve{\omega}}}{\partial x} = a\frac{\partial e^{\breve{\omega}}}{\partial x} + e^{\breve{\omega}}\frac{\partial a}{\partial x} = e^{\breve{\omega}}\left[a\frac{\partial \breve{\omega}}{\partial x} + \frac{\partial a}{\partial x}\right] = e^{\breve{\omega}}\left[\frac{\partial a\breve{\omega}}{\partial x} + (1-\breve{\omega})\frac{\partial a}{\partial x}\right] \quad (25)$$

Focusing the attention on the ω-equation 19, identity 25 can be applied to inertia and convective terms on the LHS:

$$\begin{aligned} \frac{\partial \rho\omega}{\partial t} + \frac{\partial \rho u_j \omega}{\partial x_j} = \quad & e^{\breve{\omega}}\left[\frac{\partial \rho\breve{\omega}}{\partial t} + \frac{\partial \rho u_j\breve{\omega}}{\partial x_j} + \underbrace{(1-\breve{\omega})\left(\frac{\partial \rho}{\partial t} + \frac{\partial \rho u_j}{\partial x_j}\right)}_{\text{0 for continuity}}\right] \quad = \\ & e^{\breve{\omega}}\left[\frac{\partial \rho\breve{\omega}}{\partial t} + \frac{\partial \rho u_j\breve{\omega}}{\partial x_j}\right] \end{aligned} \quad (26)$$

where $(1-\breve{\omega})\left(\frac{\partial \rho}{\partial t} + \frac{\partial \rho u_j}{\partial x_j}\right)$ vanishes because of continuity.

The diffusion term can be managed as:

$$\begin{aligned} \frac{\partial}{\partial x_j}\left[(\mu + \sigma_\omega \mu_t)\frac{\partial \omega}{\partial x_j}\right] = \frac{\partial}{\partial x_j}\left[(\mu + \sigma_\omega \mu_t) e^{\breve{\omega}}\frac{\partial \breve{\omega}}{\partial x_j}\right] = \\ (\mu + \sigma_\omega \mu_t)\frac{\partial \breve{\omega}}{\partial x_j}\frac{\partial e^{\breve{\omega}}}{\partial x_j} + e^{\breve{\omega}}\frac{\partial}{\partial x_j}\left[(\mu + \sigma_\omega \mu_t)\frac{\partial \breve{\omega}}{\partial x_j}\right] = \end{aligned}$$

$$e^{\breve{\omega}}\left[\underbrace{(\mu+\sigma_\omega\mu_t)\frac{\partial\breve{\omega}}{\partial x_j}\frac{\partial\breve{\omega}}{\partial x_j}}_{additional\ term}+\frac{\partial}{\partial x_j}\left[(\mu+\sigma_\omega\mu_t)\frac{\partial\breve{\omega}}{\partial x_j}\right]\right]$$

where an additional term appears due to the non-linearity of the transformation.

Production and destruction terms (eqs. 22 and 23) trivially becomes:

$$PROD_\omega=\frac{\tau_{ij}^R}{\mu_t}\frac{\partial u_i}{\partial x_j}-\frac{2}{3}\omega\frac{\partial u_i}{\partial x_i}\delta_{ij}=\frac{\tau_{ij}^R}{\mu_t}\frac{\partial u_i}{\partial x_j}-\frac{2}{3}e^{\breve{\omega}}\frac{\partial u_i}{\partial x_i}\delta_{ij}$$

$$DESTR_\omega=\omega^2=e^{2\breve{\omega}}$$

From previous formulas, the complete set of equations of the $k-log(\omega)$ (or $k-\breve{\omega}$) model can be re-written as:

$$\frac{\partial\rho k}{\partial t}+\frac{\partial\rho k u_j}{\partial x_j}=\frac{\partial}{\partial x_j}\left[(\mu+\sigma_k\mu_t)\frac{\partial k}{\partial x_j}\right]+S_k \tag{27}$$

$$\frac{\partial\rho\breve{\omega}}{\partial t}+\frac{\partial\rho\breve{\omega}u_j}{\partial x_j}=\underbrace{(\mu+\sigma_\omega\mu_t)\frac{\partial\breve{\omega}}{\partial x_j}\frac{\partial\breve{\omega}}{\partial x_j}}_{additional\ term}+\frac{\partial}{\partial x_j}\left[(\mu+\sigma_\omega\mu_t)\frac{\partial\breve{\omega}}{\partial x_j}\right]+S_{\breve{\omega}} \tag{28}$$

where,

$$S_k=\mu_t(PROD_k-\beta^*DESTR_k) \tag{29}$$

$$S_{\breve{\omega}}=\rho(\gamma PROD_{\breve{\omega}}-\beta DESTR_{\breve{\omega}}) \tag{30}$$

$$PROD_k=\frac{\tau_{ij}^R}{\mu_t}\frac{\partial u_i}{\partial x_j}-\frac{2}{3}e^{\breve{\omega}}\frac{\partial u_i}{\partial x_i}\delta_{ij} \tag{31}$$

$$PROD_{\breve{\omega}}=\frac{PROD_k}{e^{\breve{\omega}}}=\frac{1}{e^{\breve{\omega}}}\frac{\tau_{ij}^R}{\mu_t}\frac{\partial u_i}{\partial x_j}-\frac{2}{3}\frac{\partial u_i}{\partial x_i}\delta_{ij} \tag{32}$$

$$DESTR_k=e^{2\breve{\omega}} \tag{33}$$

$$DESTR_{\breve{\omega}}=\frac{DESTR_k}{e^{\breve{\omega}}}=e^{\breve{\omega}} \tag{34}$$

$$\mu_t=\frac{\rho\cdot max(0,k)}{e^{\breve{\omega}}}=\frac{\rho\cdot k^*}{e^{\breve{\omega}}} \tag{35}$$

where, for convenience, all terms in the $\breve{\omega}$ equation (including source) have been divided by $e^{\breve{\omega}}$ and $k^*=max(0,k)$. It should be noticed that:

- $\breve{\omega}$ can be negative, but $\omega = e^{\breve{\omega}}$ is always stricly positive.
- k can be negative, but μ_t can be re-defined according to eq. 35, so that it is always stricly positive.
- Accuracy is improved, because generally ω exhibits large variations in the domain well captured by the logarithmic function.

Wall boundary condition for $\breve{\omega}$ can be easily derived. From the theory, ω tends to infinity close to solid walls; nevertheless, it can be shown by perturbation techniques that a value of ω_{wall} greater than

$$100\frac{u_\tau^2}{\nu} = 100\frac{\tau_w}{\mu}$$

is by far sufficient to give accurate solutions. For the logarithmic variable $\breve{\omega}$, obiouvsly holds:

$$\breve{\omega}_{wall} = ln(\omega_{wall}) = ln\left(100\frac{\tau_w}{\mu}\right)$$

This $log(\omega)$ formulation has been tested succesfully; no special initial conditions are needed to achieve convergence, but constant initial values are generally enough.

2 Validation

2.1 Turbulent flow over a flate plate

2.1.1 Description

In this classical test case, air moving with uniform and constant freestream velocity, flows over a flat plate with zero pressure gradient, developing a momentum turbulent boundary layer giving rise to a velocity profile which follows the universal law of the wall.

2.1.2 Test case set-up

A 96x64 cell grid in streamwise and crosswise direction respectively, has been used for the present computation. The grid refinement at the solid boundary is such as to achieve a y^+ of the order unity. The incoming fluid flows at a speed of $6m/s$.

2.1.3 Results

All the turbulence models implemented in **Ares** have been validated against the flat plate test case. Figure 2 shows the non-dimensional velocity profiles in a *log-linear* plot. All models capture the correct slope in the log region of the boundary layer, and the S&A and $\kappa-\omega$ only are able to reproduce the linear behaviour in the laminar sublayer. The standard and RNG $\kappa-\epsilon$ models in fact make use of wall functions, which do not allow to capture the correct linear velocity profile within the laminar sublayer. The reference theoretical law of the wall in the figure is given by (see [10] pag. 640):

$$u^+ \equiv \frac{U}{U^*} = 5.85\ ln(y^+) + 5.56$$

Figure 3 compares the computed wall skin friction coefficient distributions against three semi-empirical expressions given in table 1. Both the S&A and the $\kappa-\omega$ models give the correct slope, though only the S&A model is quantitatively accurate, while the $\kappa-\omega$ overpredicts the skin friction. Solutions obtained with turbulence models with wall-function show the expected drawbacks. The not accurate behaviour of the $\kappa-\omega$ solution is due to the previously discussed model drawback related to the strong sensitivity to the ω free stream conditions. A trial-and-error procedure with different values of ω_∞ would certainly lead to "satisfactory" agreement.

CF1	$0.0262/REX**(1./7.)$
CF2	$0.0375/REX**(1./6.)$
CF3	$0.0592/REX**(1./5.)$

Table 1: semi-empirical expressions for the skin friction coefficient

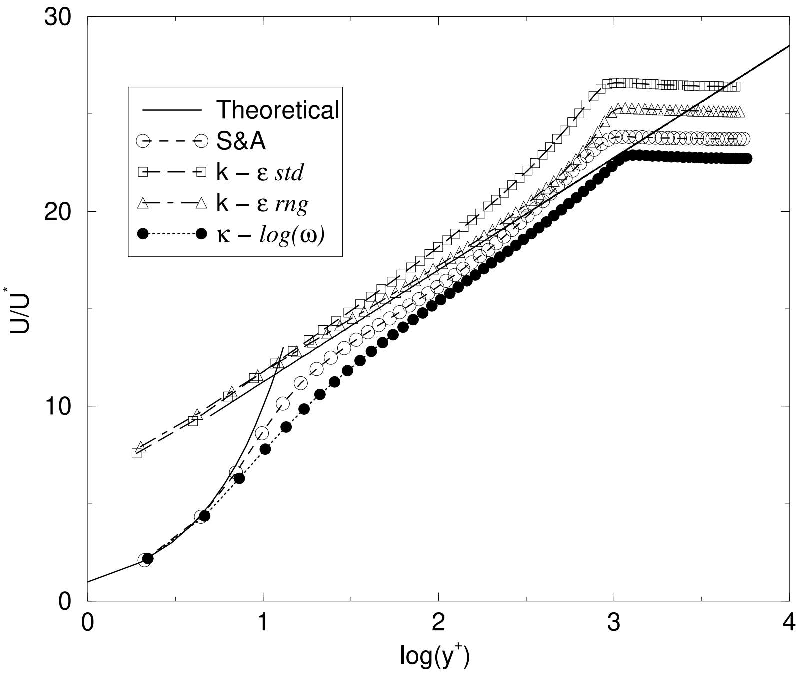

Figure 2: Dimensionless velocity profile at solid wall

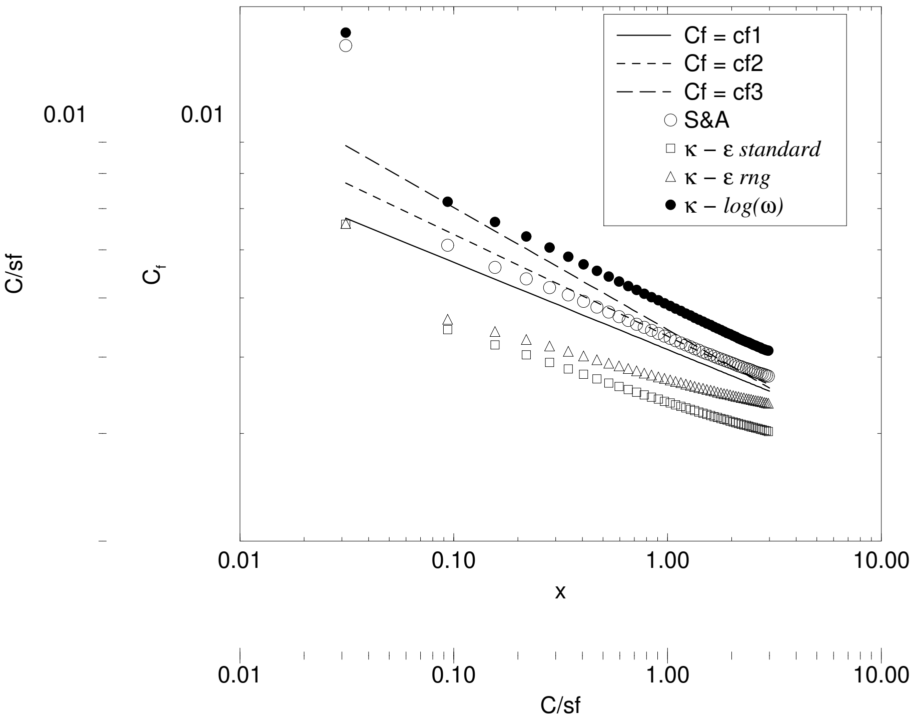

Figure 3: Skin friction factor along the flate plate

2.2 Backward Facing Step

2.2.1 Description

The backward facing step computed by Moin [11] with Direct Numerical Simulation (DNS) has been chosen as the second benchmark test case. Of particular relevance is the correct prediction of the position of the reattachment point, estimated by Moin to be at 6.28 x/h. Figures 4 shows the problem's geometry.

2.2.2 Test case set-up

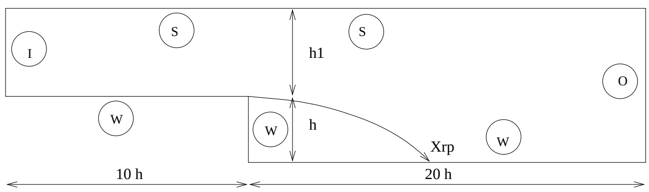

Figure 4: Step geometry

Computational domain, shown in the same figure 4, extends from 10 $\frac{x}{h}$ upstream the step to 20 $\frac{x}{h}$ downstream, in order to ensure the uniformity of the flow field at the outlet section. A two block grid have been used. The number of cells for the two blocks upstream and downstream the step, was 48 x 40 and 64 x 80 respectivelly. The grid stretching at the walls allows the use of all models, with the first grid spacing of order 10^{-5}. Table 2 lists the boundary conditions used and table 3 reports the main parameters used for the computation.

I	Inlet
O	Pressure Outlet
W	Adiabatic Solid Wall
S	Symmetry Plane

Table 2: Boundary conditions

The inlet velocity profile imposed is taken from DNS data. All two-equation models make use of inlet turbulent kinetic energy (κ) profile, also from DNS data. The second turbulent variable (ϵ or ω) is extrapolated from the inetrior domain. It is

Courant number (CFL)	1
Numerical scheme	Quick
Linear system solution method	CGS
Preconditioning	ADI

Table 3:

the authors' opinion that, whenever velocity and turbulence profiles are available for boundary layer inlet boundaries, extrapolation of the second turbulent variable allows the turbulent fields to reach their own equilibrium and insure correct results. In the case of the S&A model, the turbulent variable ν has been estrapolated from the interior of the domain. Again, the idea is that, whenever a boundary layer velocity field is imposed at the inlet (and so the vorticity field) this procedure is a possible valuable alternative to imposing a free stream (somehow arbitrary) value.

2.2.3 Results

Figures 5, 6 8 and 7 show the skin friction coefficient ($Cf = \tau_w / 0.5 \rho U_0^2$) computed at solid wall behind the step.

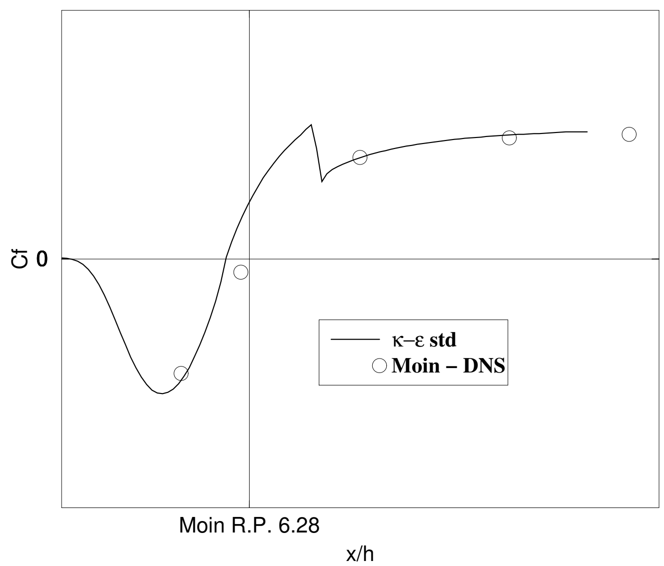

Figure 5: Skin friction coefficient standard $\kappa - \epsilon$ model

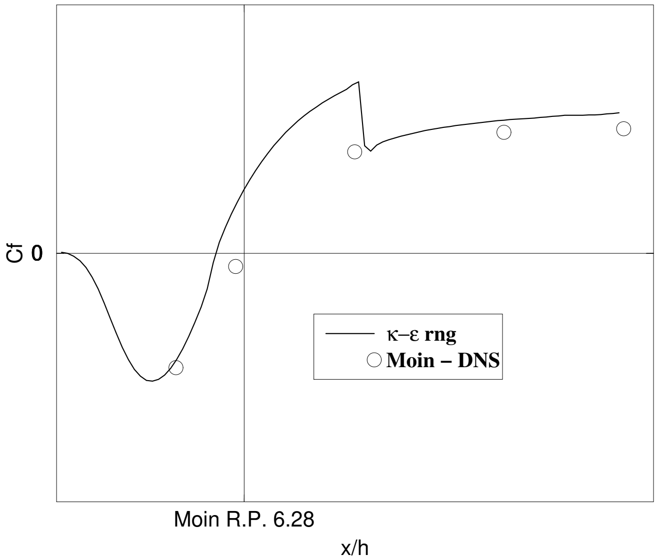

Figure 6: Skin friction coefficient RNG $\kappa - \epsilon$ model

Examination of figures 5 to 8 permits to observe how the existence of a small vortex right behind the step is captured by the S&A and $\kappa - log(\omega)$ models only. This recirculation zone extends to about 1.2 x/h, value which is in agreement with DNS result. Both $\kappa - \epsilon$ models present a sort of singularity in the computed values of the skin-friction coefficient. This behaviour is not present in both the S&A and $\kappa - log(\omega)$ computations and it is probably due to some wall function effect, not fully understood. Table 4 shows the predicted position of the reattachment point, evaluated as the point at which τ_w changes sign.

Turbulence model	Reattachment Point position [x/h]
$\kappa - \epsilon$ Standard	5.500
$\kappa - \epsilon$ RNG	5.440
S&A	5.748
$\kappa - log(\omega)$	6.54

Table 4: Computed reattachment point position; DNS simulation 6.28

Figures 9, 10, 11 and 12 show the dimensionless profiles of streamwise velocity and Reynolds stresses at four different locations behind the step. All models give

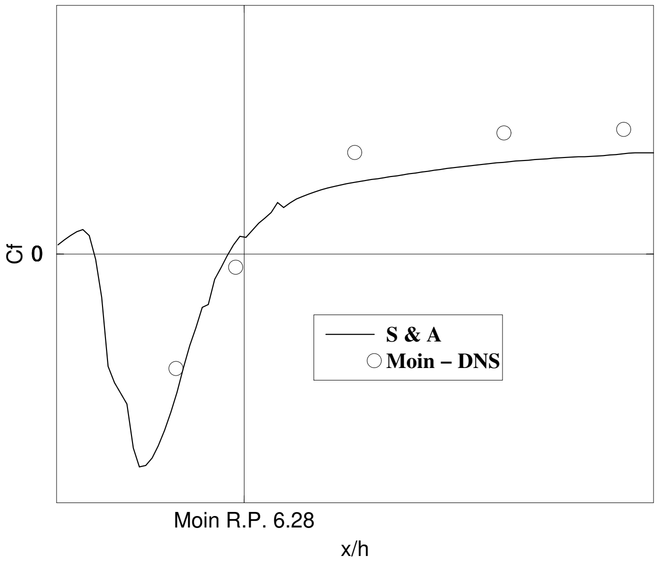

Figure 7: Skin friction coefficient S&A model

satisfactory results both in terms of velocity and Reynolds stresses. The S&A model appears slightly less accurate in the velocity profile prediction, whereas the Reynolds stresses value is more correctly estimated in the region of y/h ≥ 1, where both the $\kappa - \epsilon$ models undershoot the actual value.

All models but the $\kappa - log(\omega)$ predict an early reattachment. In this boundary layer like problem, the $\kappa - log(\omega)$ model shows its power in accurately capturing the features of such a typical recirculating test case, and does not show up the mentioned free stream sensitivity. Rescaling the streamwise profile locations at the same distances from the whatever calculated reattachment point, allows to evaluate the results from a different point of view (figures 13, 14, 15 and 16).

Finally, in figures 17 the velocity contour plots are shown.

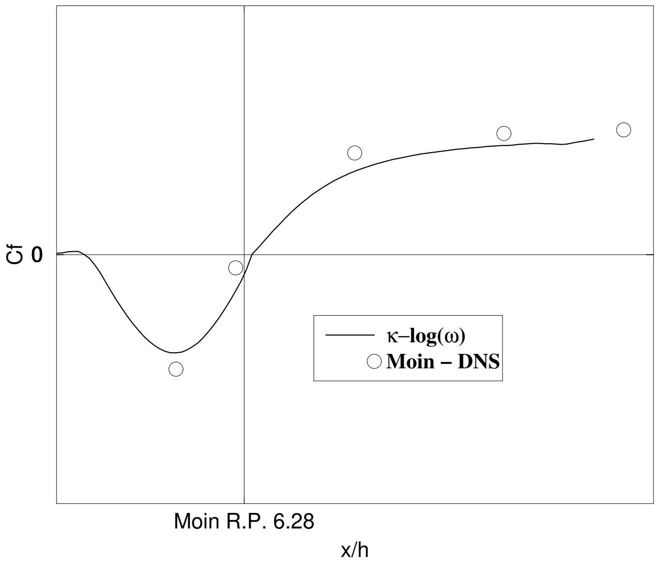

Figure 8: Skin friction coefficient $\kappa - log(\omega)$ model

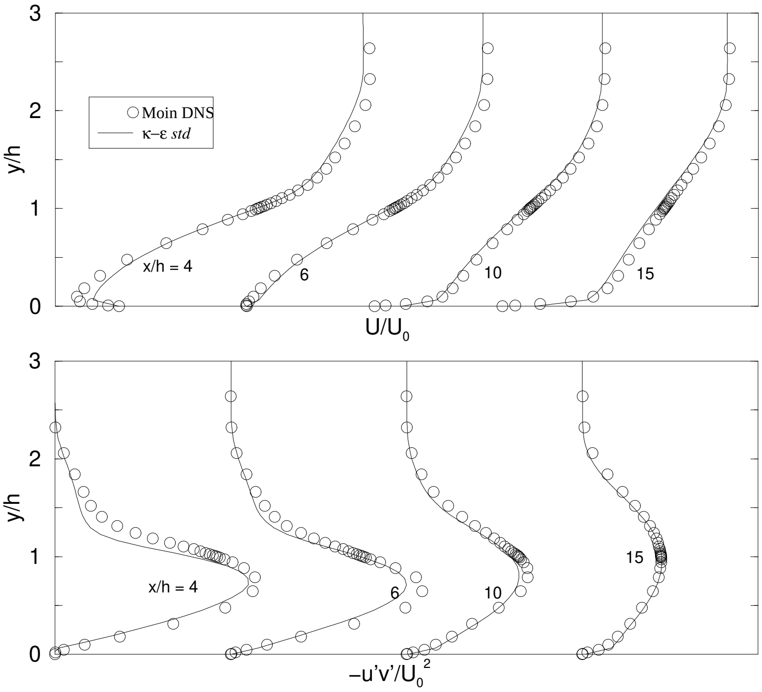

Figure 9: Velocity and Reynolds stress profiles standard $\kappa - \epsilon$ model

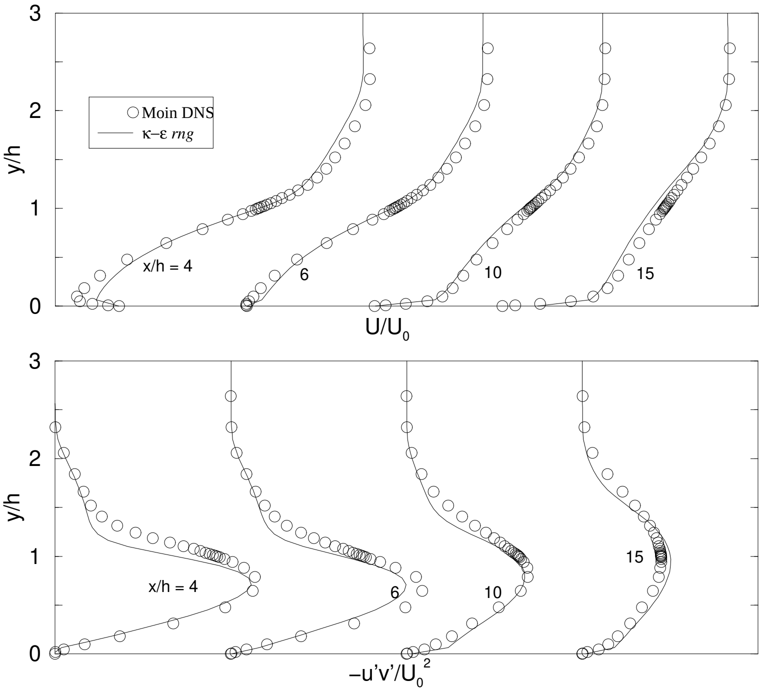

Figure 10: Velocity and Reynolds stress profiles RNG $\kappa - \epsilon$ model

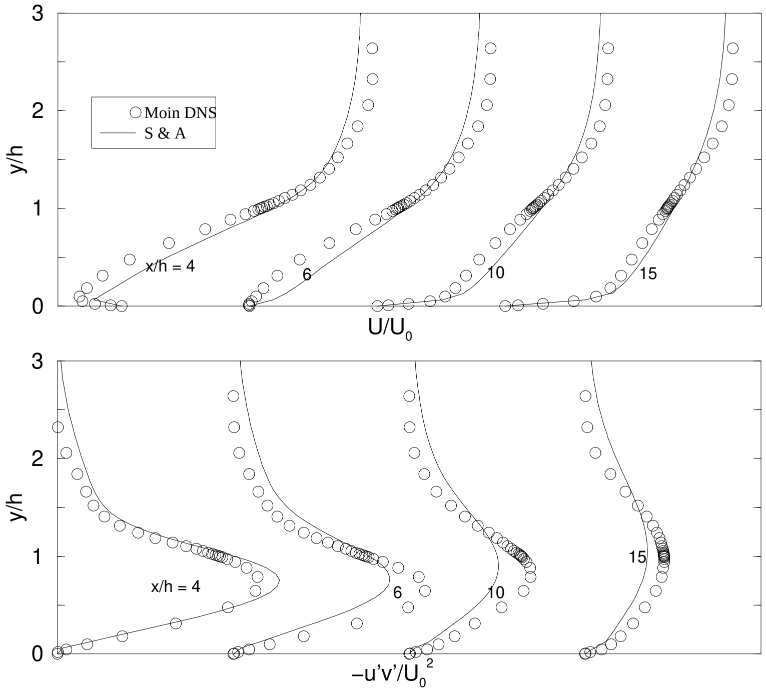

Figure 11: Velocity and Reynolds stress profiles S&A model

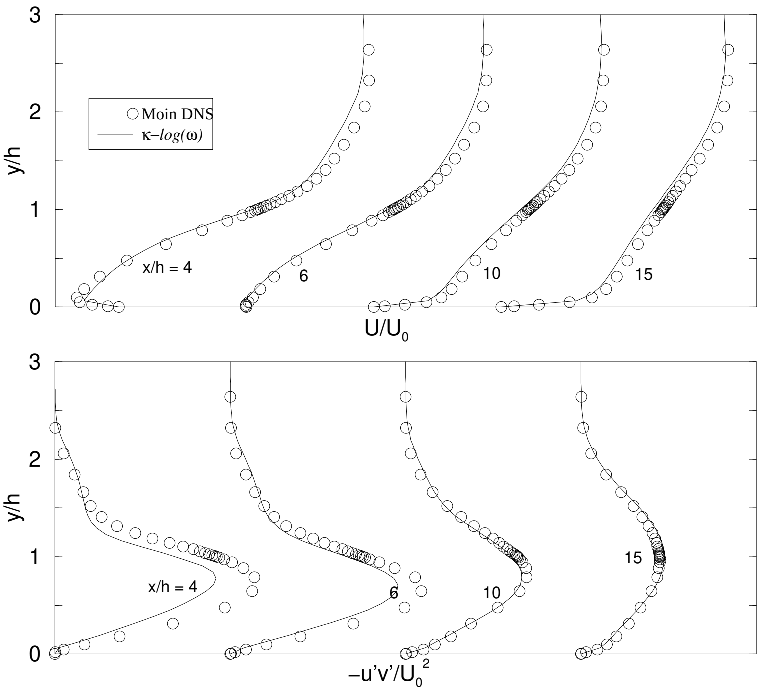

Figure 12: Velocity and Reynolds stress profiles $\kappa - log(\omega)$ model

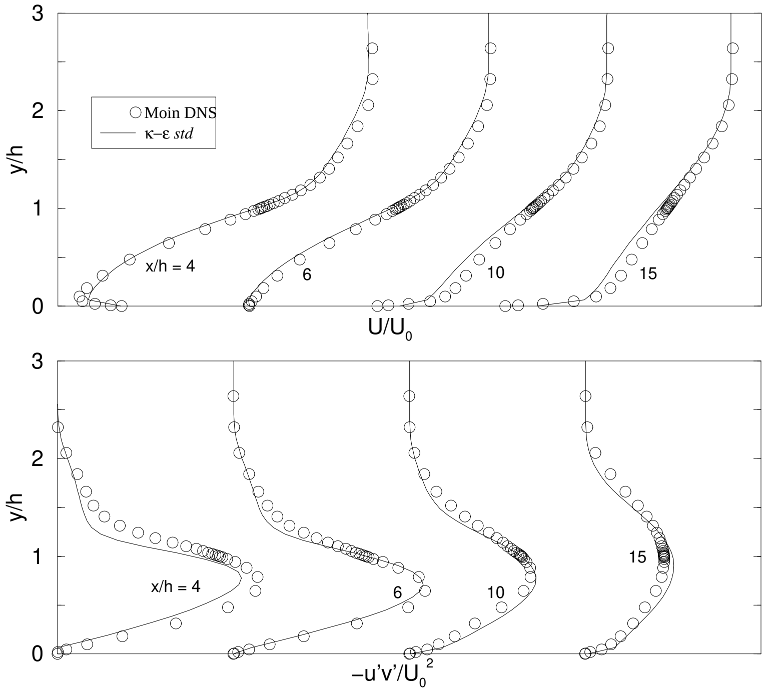

Figure 13: Rescaled Velocity and Reynolds stress profiles standard $\kappa - \epsilon$ model

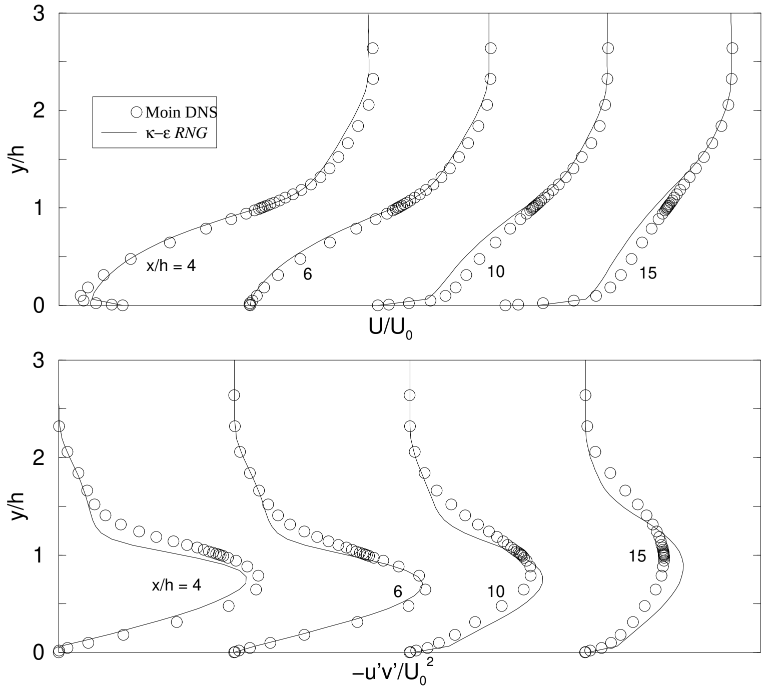

Figure 14: Rescaled Velocity and Reynolds stress profiles RNG $\kappa - \epsilon$ model

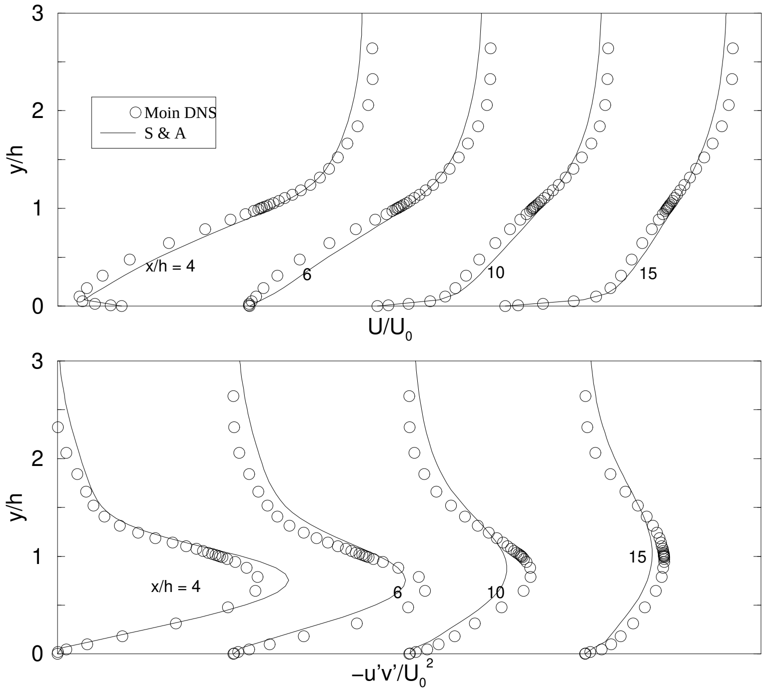

Figure 15: Rescaled Velocity and Reynolds stress profiles S&A model

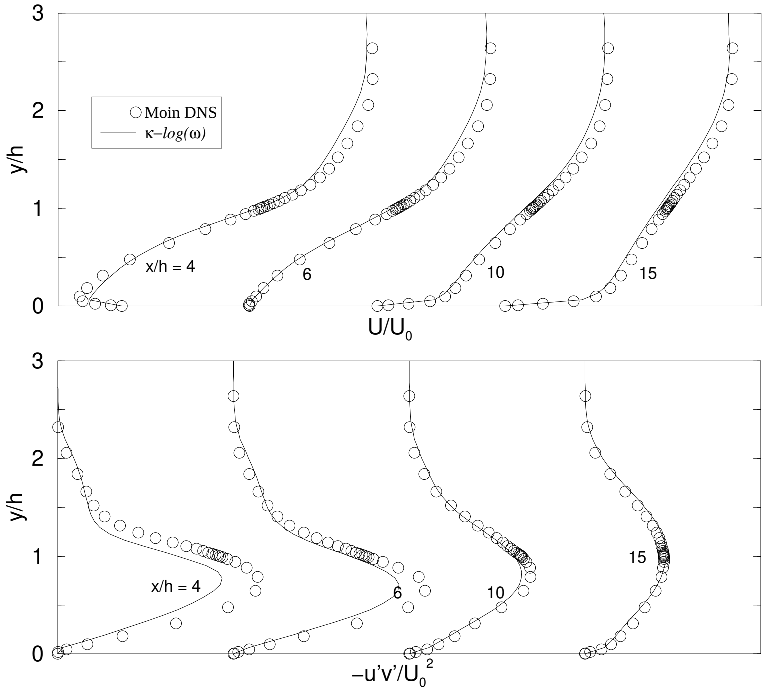

Figure 16: Rescaled Velocity and Reynolds stress profiles $\kappa - log(\omega)$ model

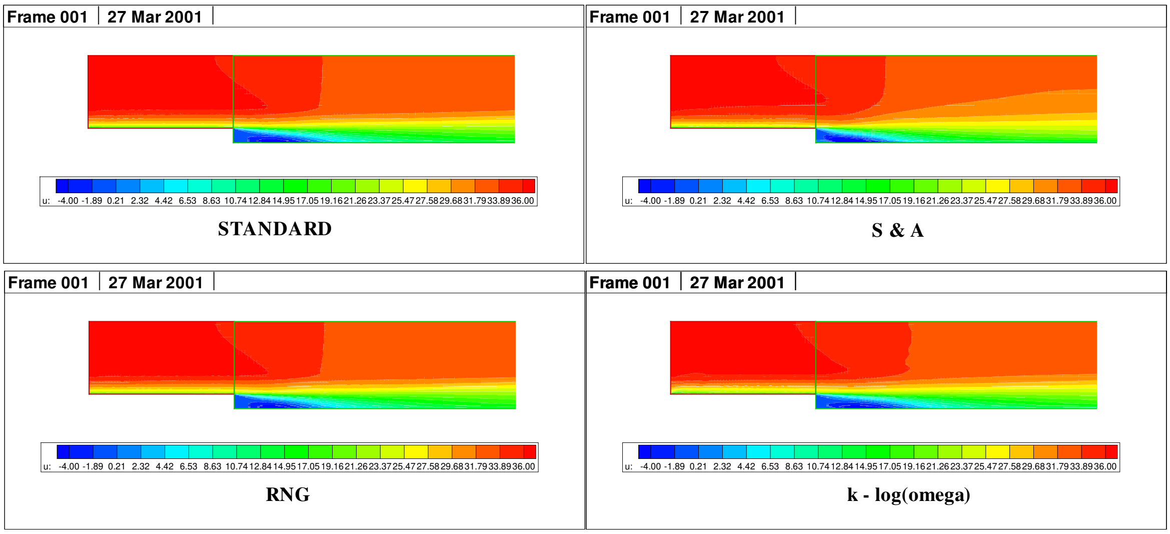

Figure 17: Velocity contour plots

2.3 Moreau Combustor

2.3.1 Description

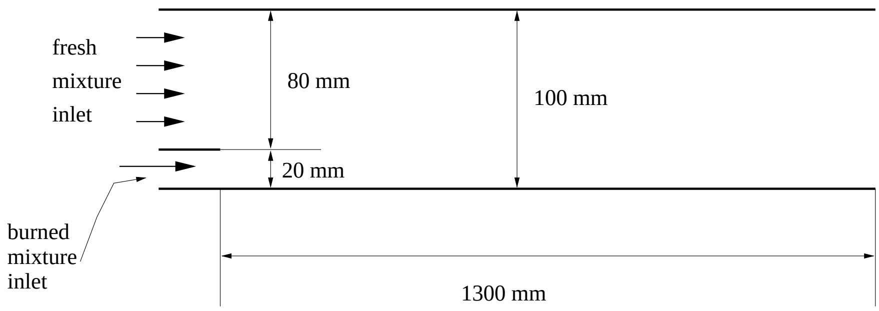

Figure 18: Combustor's geometry

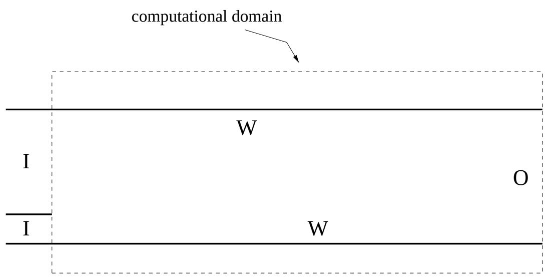

Figure 19: Used boundary conditions: **I** inlet, **O** pressure outlet, **W** adiabatic solid wall.

The Moreau combustor is an eperimental planar combustion chamber of rectangular cross section. The chamber is 100 [mm] height and it is fed through two separated inlets, as shown in figure 18. An omogeneous fresh mixture of CH_4 and air ($f = 0.04832$, $\phi = 0.87$) enters the combustor through the upper inlet with velocity of 65 [m/s] and temperature of 600 [K]. A burned mixture of CH_4 and air with the same composition feeds the combustor through the lower inlet for flame stabilization purposes, with velocity of 108 [m/s] and temperature of 2000 [K]. Experimental tests have been carried out at ONERA (F) by Moreau et al. [12, 13].

The flow's regime is turbulent and straigth, free of any recirculating regions.

	burned mixture inlet A	fresh mixture inlet B
u [m/s]	108.0	65.0
v [m/s]	0.0	0.0
turbulence intensity	21%	12%
integral lenght	0.0014	0.0056
Φ	0.87	0.87
f	0.04832	0.04832
Y_{CH_4}	0.0	0.04832
Y_{O_2}	0.0	0.22174
Y_{CO_2}	0.13255	0.0
Y_{H_2O}	0.10852	0.0
Y_{N_2}	0.72994	0.72994

Table 5: Inlet conditions

2.3.2 Test case set-up

The used grid has 4,200 cells (105 x 40) and it is slighty streched at solid walls. Table 6 shows the main settings used with both the turbulence models.

Courant number (CFL)	10
Numerical scheme	2nd order centered
Linear system solution method	CGS
Preconditioning	ADI
Combustion model	Premixed - TFC

Table 6: Main parameters used for the calculation

2.3.3 Results

Figures 20, 21, 22 and 23 show the logarithm of normalized residuals root mean square vs iteration's number. for the standard $\kappa - \epsilon$, the RNG $\kappa - \epsilon$, the S&A and the $\kappa - \omega$ model respectively. The $\kappa - \omega$ model shows a slower convergence, as any other low-Reynolds two-equation model would do.

Figure 24 shows the eddy viscosity color map for the same four models. Results are very similar to each other and qualitatively correct.

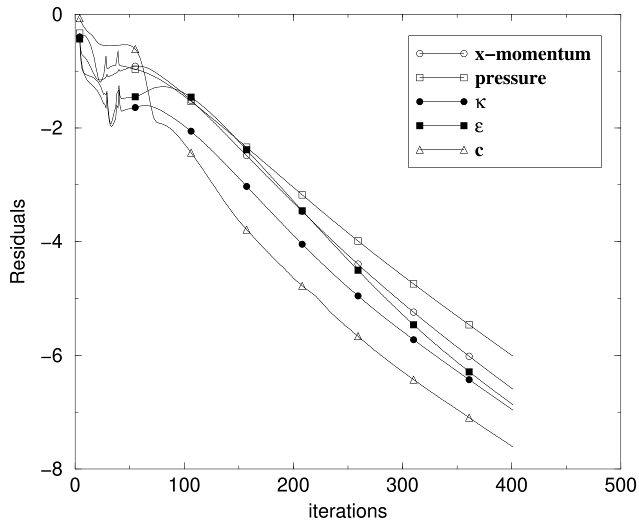

Figure 20: Convergence of standard model

Figure 25 shows the computed temeperature profiles at 222[mm] and 522[mm] from inlet. First of all it has to be noted that all models give a maximum temperature of 2240[K], whereas the experimental data value is 2000[K]. This is due to the limitation of the TFC model which necessarily makes use of the adiabatic flame temperature (2240[K]) whenever the value of the progress variable is equal to one. In other words, with the TFC model it is not possible to set the burned inflow ($c = 1$) at a temperature different from the corresponding adiabatic flame temperature. These issues have been discussed in [14]. The best agreement is obtained with the $\kappa - \omega$ model, though affected by the model limitation.

Figure 26 shows velocity profiles at three different locations downstream the combustor inlet, namely at 151 [mm], 351 [mm] and 650 [mm] from the inlet section. The $\kappa - \omega$ model shows the best agreement, particularly at the first section, where the other three models fail to reproduce the velocity profile. The S&A model shows results similar to those obtained with the two $\kappa - \epsilon$ models, or a little worse, which seems to suggest an improved coupling with the combustion model.

The velocity field carries however the errors generated by the progress variable equation (i.e. the combustion model). It is clear in fact that a wrong prediction of the progress variable c field, generates wrong temperature as well as wrong density fields. This because, in the TFC model, $T = T(c)$ and $\rho = \rho(T) \ \Rightarrow \ \rho = \rho(c)$. As

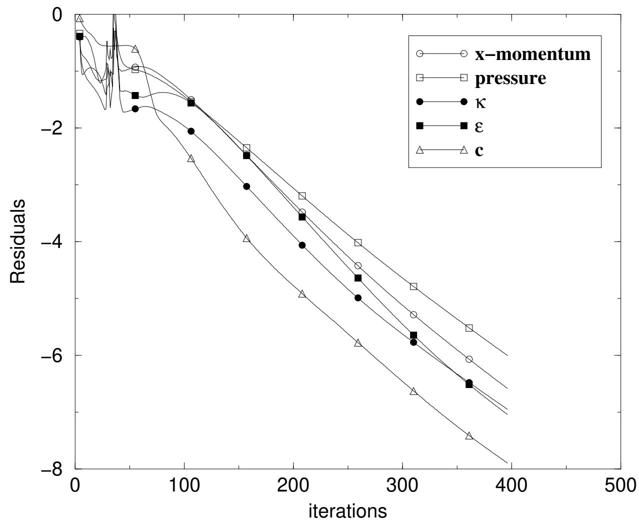

Figure 21: Convergence of RNG model

a consequence, the velocity field is also affected by the error because the continuity equation ties together density and velocity. In other words, analysis of the velocity fields does not add any new information about the model performance.

Other turbulent reactive test cases are however necessary for validating the performance of all models before drawing conclusions and eventually modifying the models implementation.

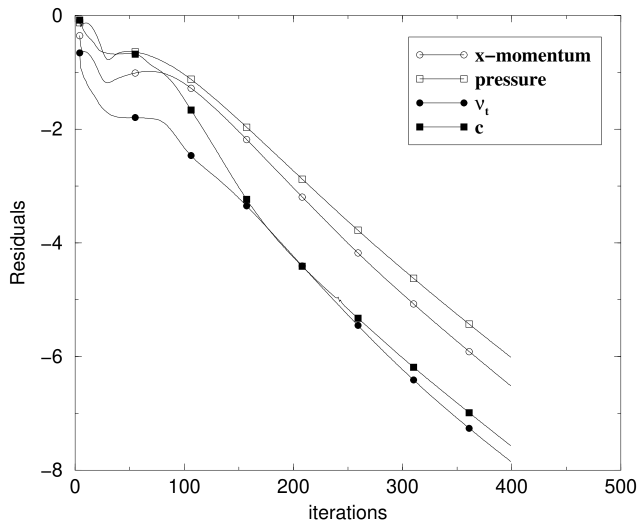

Figure 22: Convergence of S&A model

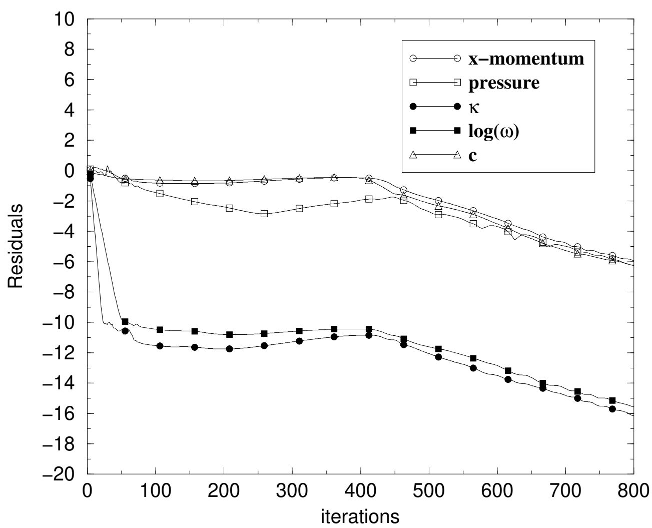

Figure 23: Convergence of $\kappa - \omega$ model

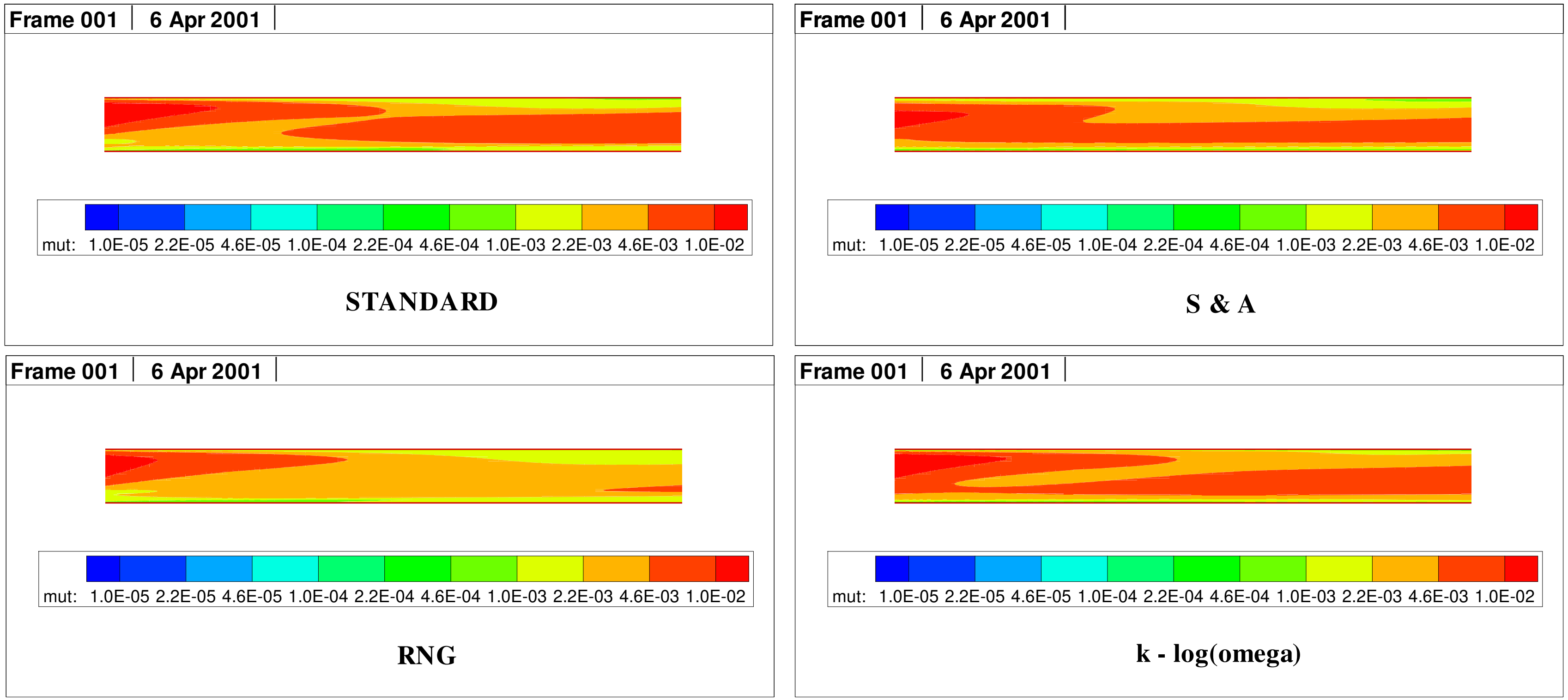

Figure 24: calculated eddy viscosity fields for all models

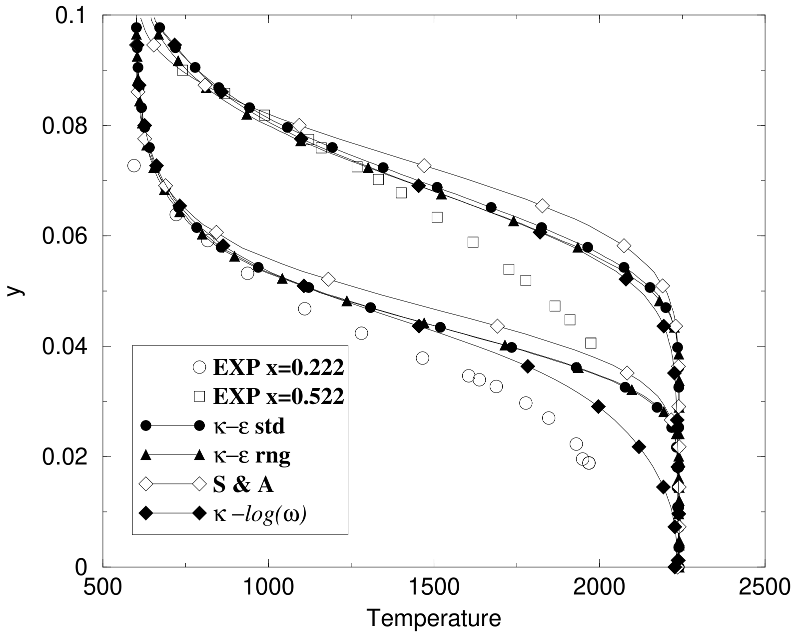

Figure 25: Temperature profiles

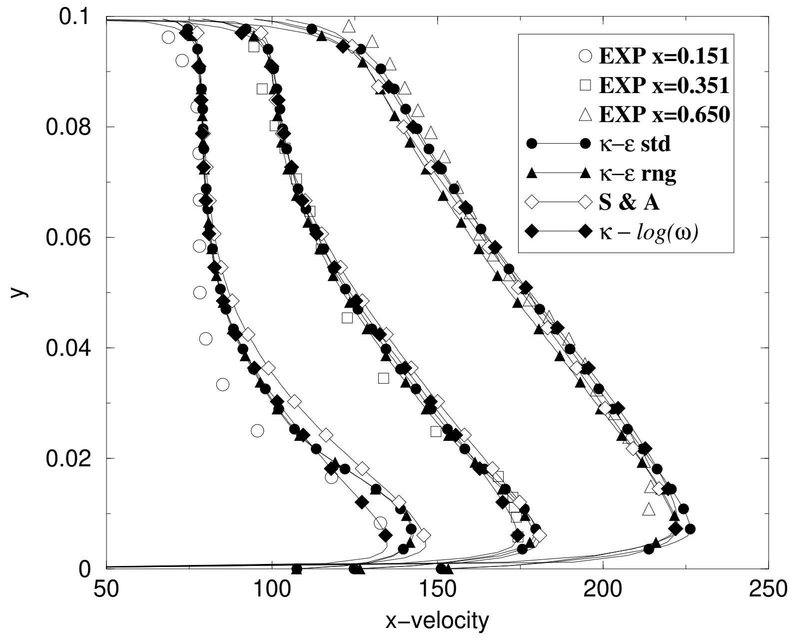

Figure 26: Velocity profiles

References

[1] Yakhot V. and Orszag S.A. Renormalization group analysis of turbulence theory. i. basic theory. *J. Sci. Comput.*, 1(3), 1986.

[2] P. R. Spalart and S.R. Allmaras. A one-equation turbulence model for aerodynamic flows. *La Recherche Aerospatiale*, 1:5–21, 1992.

[3] M. Papadakis, V. Lall and K. A. Hoffmann. Performance of turbulence models for planar flows: A selected review. In *12th AIAA Applied Aerodynamics Conference*, pages 1–45. American Institute of Aeronautics and Astronautics, 1994.

[4] J. E. Bardina, P. G. Huang, and T. J. Coakley. Turbulence modeling validation, testing and development. NASA Technical Memorandum 110446, pages 1–88. National Aeronautics and Astronautics Administration, April, 1997.

[5] Linda D. Kral, Mori Mani, and John A. Ladd. Application of turbulence models for aerodynamic and propulsion flowfields. *AIAA Journal*, 34(11):2291–2298, November 1996.

[6] Barbato M.C. Zimont V.L. "Modellizzazione e Teorizzazione per Combustione Premiscelata e Parzialmente Premiscelata". Technical Report 99/71, CRS4, December 1999.

[7] Talice M. Barbato M. and Trotta L. "Validazione dello Stato dell'Arte nella Simulazione di Processi Combustivi". Technical Report 99/17, CRS4, October 1999.

[8] Wilcox D.C. Reassessment of the Scale-Determining Equation for Advanced Turbulence Models. *AIAA J.*, 26(11):1299–1310, 1988.

[9] Di Piazza I. and Mulas M. "Development and Improvement of $\kappa-\omega$ Turbulence Models in the CFD Code Karalis". Technical report, CRS4, March 2001.

[10] Schlichting H. *Boundary-Layer Theory*. Mc Graw Hill, 1979.

[11] Le, H., Moin, P., and Kim, J. Direct Numerical Simulation of Turbulent Flow over a Backward Facing Step. *J. of Fluid Mechanics*, 330:349–374, 1997.

[12] Moreau, P., and Boutier, A. Laser Velocimetry Measurements in a Turbulent Flame. In *Sixteenth Symposium (Int.) on Combustion*, pages 1747–1756. The Combustion Institute, 1976.

[13] Moreau, P.,. Turbulent Flame Development in a High Velocity Premixed Flow. *AIAA Paper 77-49, AIAA 18th Aerospace Science Meeting*, Jan. 24-25 1977, Los Angeles, CA.

[14] Mulas M. "On the Numerical Simulation of Premixed Combustion Flows with a Density-based Formulation". Technical report, CRS4, February 2000.